Planetary and Space Science 84 (2013) 20–27

Contents lists available at SciVerse ScienceDirect

Planetary and Space Science

journal homepage: www.elsevier.com/locate/pss

Simulation and results on real-time positioning of Chang'E-3 rover with the same-beam VLBI observations

Erhu Wei [a], Shuanggen Jin [b,*], Hongzhou Yang [a], Xuechuan Li [a], Hongye Gu [a], Zhiqiang Li [a], Jinling Li [b], Koji Matsumoto [c], Jingnan Liu [d]

[a] School of Geodesy and Geomatics, Wuhan University, Wuhan 430079, China
[b] Shanghai Astronomical Observatory, Chinese Academy of Sciences, Shanghai 200030, China
[c] RISE Project, National Astronomical Observatory of Japan, Iwate 023-0861, Japan
[d] GNSS Research Center, Wuhan University, 129 Luoyu Road, Wuhan 430079, China

ARTICLE INFO

Article history:
Received 3 January 2013
Received in revised form
12 March 2013
Accepted 12 April 2013
Available online 6 May 2013

Keywords:
Lunar exploration
VLBI
Same-beam interferometry
Kinematic positioning

ABSTRACT

The real-time and high precision positioning of the lunar rover vehicle is an important step for lunar exploration and science. SBI (same-beam interferometry) is the differential very long baseline interferometry (VLBI) technology, which can be used in lunar exploration with its high precision and stability. In this paper, the relative positioning model of the lunar rover vehicle (LRV) to lunar module (LM) based on the SBI and extended kalman filtering (EKF) is developed and presented. Using the current Chinese VLBI network and the planed Chang'E-3, SBI observation data with an attainable precision of picoseconds and a sample interval of 4 s are simulated. The LRV's relative position to the LM is then estimated by the least squares adjustment, EKF and an adaptive EKF, respectively. Results show that the Adaptive EKF performs the best real-time solutions with the accuracy of 1.86 m in *X* direction, 0.33 m in *Y* direction and 0.09 m in *Z* direction, which can provide a good reference for real-time positioning of planed Chang'E-3 rover.

© 2013 Elsevier Ltd. All rights reserved.

1. Introduction

Since the successful landing of the Apollo 11 mission in 1969, exploration of moon has been intensified and carried out by a number of missions, e.g., recent SELenological and ENgineering Explorer "KAGUYA" (SELENE), Chang'E-1, Chandrayaan-1, and Lunar Reconnaissance Orbiter/Lunar CRater Observation and Sensing Satellite (LRO/LCROSS) (Jin, 2012; Jin et al., 2013). The Chinese lunar exploration project consists of three stages: surrounding, landing and returning. Following the successful launch of the Chinese lunar probes Chang'E-1 (CE-1) and Chang'E-2 (CE-2), the launch of the Chang'E 3 (CE-3) probe is planned to be launched in the latter half of 2013. There are two probes in the CE-3 mission: LRV and LM, whose primary objectives are the g eological, geochemical and geophysical explorations of the landing area, and establishment of the astronomical observatory (Ouyang, 2004). The detecting equipments onboard require a tracking and controlling system that simultaneously manages multi-explorers. Thus, one of key issues is how to determine the relative position between the LRV and LM with a high accuracy (Liu et al., 2010).

SBI is a kind of differential VLBI (very long baseline interferometry) technology, which can provide extremely accurate relative position measurements in the plane-of-sky and complement the line-of-sight information from Earth-based Doppler and range measurement. The atmosphere, ionosphere, and receiver influences can be almost removed in SBI observations and the difference in time delay can be directly obtained with an accuracy of several picoseconds from the correlation phase (Liu et al., 2010).

Single-frequency SBI has been used in tracking the Apollo 16 and 17 lunar rovers with a relative positioning accuracy of 25 m. The Japanese lunar exploration mission-SELENE has been launched on 14 September, 2007 with carrying a tracking system called multi-frequency same-beam differential VLBI between two sub-satellites, which can obtain the differential phase delay directly to solve the ambiguity problem and to provide an accurate result. The contributions of the SBI in spacecraft precision orbit determination and lunar gravity field solution have been investigated in the SELENE mission by GEODYN II/SOLVE. Yan et al. (2011) showed significant improvements in accuracy of low and medium degree coefficients of lunar gravity field model obtained from combination of two way range and Doppler and the same beam VLBI measurements than only two way range and Doppler data, and the accuracy of precision orbit determination can reach the level of meter. The SBI can also be used as a tool for the investigation of the lunar interior with three or more landers on the lunar surface (Gregnanin et al., 2012).

In this paper, the effect of SBI in the relative positioning is simulated and tested for LRV and LM capsule landing on the moon during the coming Chang'E-3 mission of Chinese lunar exploration.

* Corresponding author. Tel.: +86 21 34775292; fax: +86 21 64384618.
E-mail addresses: sgjin@shao.ac.cn, sg.jin@yahoo.com (S. Jin).

0032-0633/$ - see front matter © 2013 Elsevier Ltd. All rights reserved.
http://dx.doi.org/10.1016/j.pss.2013.04.005

Although scientists have tested the related SBI, but most took the least squares adjustment during the data processing, which cannot achieve a real-time solution to provide navigation information. Here, a newly relative positioning model based on EKF and SBI is introduced and a series of simulation experiments are performed. Because the actual positions and velocities are known, the accuracy and results of the relative positioning is assessed from the difference between the actual orbit and the solved one.

2. Theory of relative positioning with SBI

The differential VLBI (ΔVLBI) technique has played a crucial role in previous lunar exploration because it only needs a downlink signal with providing a high accuracy for the angle and angle rate. The previous observations of lunar probes showed that the measurement accuracy of ΔVLBI depended on the consistent degree between the radio source and the lunar probe and sometimes the desired nearby radio source could not be found during the motion of the lunar probe (Li et al., 2010). However, for a lunar probe on the surface of the moon, the LM can be regarded as the radio source. In addition, because the LRV and LM are only a few kilometers apart, their angle distance is smaller than 0.001°. Thus, the transmission paths of the signals from the LRV and LM are very similar. Using the difference method, the atmospheric and ionospheric delays, clock errors and instrument errors can be greatly degraded, so SBI can get a high accuracy with several picoseconds. The basic theory of SBI is shown in Fig. 1 (Dong et al., 2010).

The SBI technique is actually derived from ΔVLBI with two spacecrafts, whose angle from the earth center is very small, so it can observe in the same main beam of a VLBI antenna. By using two VLBI antennas to observe the two spacecrafts simultaneously, a differential interference observation, called Δ*DOR* (delta differential one-way ranging), can be obtained (Thornton and Border, 2000). Due to the high precision of the observation, SBI can accurately determine the relative position of the LRV and LM.

The *DOR* delay is mathematically equivalent to the time difference of the signal wavefront of the LRV arriving at the two ground VLBI antennas at one reference time. Δ*DOR* is the delay difference between the LRV and LM. As Fig. 1 shows, Δ*DOR* can be expressed by Eq. (1).

$$\tau(t)=(\tau_4-\tau_3)-(\tau_2-\tau_1) \tag{1}$$

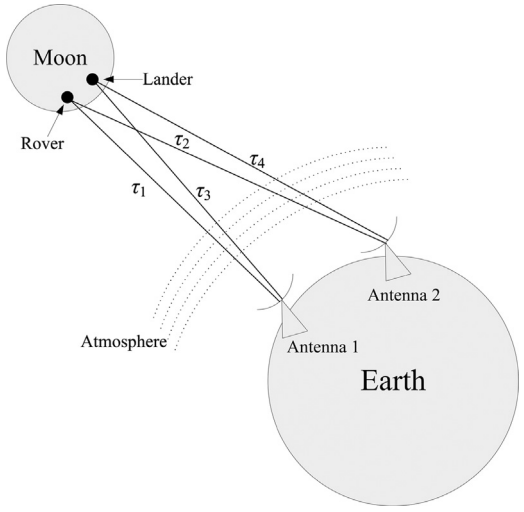

Fig. 1. The geometry of same-beam interferometry.

3. Kinematic positioning model and method

3.1. State and observation equations

The lunar surface detector does not involve a complicated dynamic model, but a kinematic model for its movement is constrained to the surface, which makes the establishment of the state equation much easier. Assume that the system state vector is as Eq. (2) at the moment k.

$$\hat{X}(k)=\left[\hat{x}_{ml}(k)\quad \hat{y}_{ml}(k)\quad \hat{z}_{ml}(k)\,\hat{x}_{ml}(k)\hat{y}_{ml}(k)\hat{z}_{ml}(k)\right]^T \tag{2}$$

In Eq. (2), the first three items on the left equation are the three-dimensional relative position of the LRV to the LM and the last three are the three-dimensional velocities of the lunar rover, which all are described in the moon-centered–moon-fixed coordinate system. In this paper, the state equation is deduced based on the simulated uniform circular motion, and then the state equation from epoch K−1 to epoch K can be expressed as following Eq. (3) :

$$\hat{X}(K)=\begin{bmatrix} \frac{\cos(w\cdot T\cdot K)-1}{\cos(w\cdot T\cdot(K-1))-1} & 0 & 0 & 0 & 0 & 0\\ 0 & \frac{\sin(w\cdot T\cdot K)}{\sin(w\cdot T\cdot(K-1))} & 0 & 0 & 0 & 0\\ 0 & 0 & 1 & 0 & 0 & 0\\ 0 & 0 & 0 & \frac{\sin(w\cdot T\cdot K)}{\sin(w\cdot T\cdot(K-1))} & 0 & 0\\ 0 & 0 & 0 & 0 & \frac{\cos(w\cdot T\cdot K)}{\cos(w\cdot T\cdot(K-1))} & 0\\ 0 & 0 & 0 & 0 & 0 & 1 \end{bmatrix} \times\hat{X}(K-1)+W(K-1) \tag{3}$$

where $W(k)$ is the system noise vector, w is the angular velocity and T is the sample interval. Provided than the position vector of the LRV at time t is $\vec{r}_m(t)$ and the position vector of the LM is $\vec{r}_l(t)$, the signal wavefronts of the LRV and LM arrive at the VLBI antenna 1 after $t_{r,m}$and $t_{r,l}$, respectively. The position vectors of the LRV and LM are now $\vec{r}_1(t+t_{r,m})$ and $\vec{r}_1(t+t_{r,l})$. The same wavefronts arrive at the VLBI antenna 2 at time $t+t_{r,m}+\tau_m$ and $t+t_{r,l}+\tau_l$, then the station position vectors become $\vec{r}_2(t+t_{r,m}+\tau_m)$ and $\vec{r}_2(t+t_{r,l}+\tau_l)$, respectively. So the observation equation at time t is shown as

$$\begin{aligned} c\Delta\tau(t)=&(|\vec{r}_2(t+t_{r,m}+\tau_m)-\vec{r}_m(t)|-|\vec{r}_1(t+t_{r,m})-\vec{r}_m(t)|)\\ &-(|\vec{r}_2(t+t_{r,l}+\tau_l)-\vec{r}_l(t)|-|\vec{r}_1(t+t_{r,l})-\vec{r}_l(t)|) \end{aligned} \tag{4}$$

where c is the speed of light, subscripts m and l represent the LRV and LM, respectively. In reality, the delay of the observation is also subject to a clock error, the instrument delay error, troposphere and ionosphere delay errors as well as the impact of random error (Huang, 2006). Assuming that the sum of the aforementioned impacts is τ_{error}, Eq. (4) can be expressed as follows:

$$\begin{aligned} c\Delta\tau(t)=&(|\vec{r}_2(t+t_{r,m}+\tau_m)-\vec{r}_m(t)|-|\vec{r}_1(t+t_{r,m})-\vec{r}_m(t)|)\\ &-(|\vec{r}_2(t+t_{r,l}+\tau_l)-\vec{r}_l(t)|-|\vec{r}_1(t+t_{r,l})-\vec{r}_l(t)|)\\ &+(\Delta_{error,m}-\Delta_{error,l}) \end{aligned} \tag{5}$$

For the sake of brevity, the time argument in Eq. (4) is ignored in the derivation of the next formula. The position vectors of the VLBI stations 1 and 2, and the LRV and LM, are respectively set as follows:

$$\begin{cases} \vec{r}_1=\left[x_1\quad y_1\quad z_1\right]^T\\ \vec{r}_2=\left[x_2\quad y_2\quad z_2\right]^T\\ \vec{r}_m=\left[x_m\quad y_m\quad z_m\right]^T\\ \vec{r}_l=\left[x_l\quad y_l\quad z_l\right]^T \end{cases} \tag{6}$$

The distances between the lunar surface detectors and VLBI stations are expressed as

$$\begin{cases} d_{1,m}=\sqrt{(x_1-x_m)^2+(y_1-y_m)^2+(z_1-z_m)^2} \\ d_{2,m}=\sqrt{(x_2-x_m)^2+(y_2-y_m)^2+(z_2-z_m)^2} \\ d_{1,l}=\sqrt{(x_1-x_l)^2+(y_1-y_l)^2+(z_1-z_l)^2} \\ d_{2,l}=\sqrt{(x_2-x_l)^2+(y_2-y_l)^2+(z_2-z_l)^2} \end{cases} \tag{7}$$

So, the observation equation can be expressed as in (8).

$$c\Delta\tau=(d_{2,m}-d_{1,m})-(d_{2,l}-d_{1,l}) \tag{8}$$

The above equation is a nonlinear observation equation, so it can be expanded by Taylor series around the one-step prediction —$\hat{X}(k/k-1)$. After ignoring the second order and higher order terms, it can be expressed as

$$\begin{aligned} c\Delta\tau=&\left[(d_{2,m}-d_{1,m})-(d_{2,l}-d_{1,l})\right]|_{\hat{X}(k/k-1)} \\ &+\frac{\partial c\Delta\tau}{\partial x_m}|_{\hat{X}(k/k-1)}(\hat{x}_m(k)-\hat{x}_m(k/k-1)) \\ &+\frac{\partial c\Delta\tau}{\partial y_m}|_{\hat{X}(k/k-1)}(\hat{y}_m(k)-\hat{y}_m(k/k-1)) \\ &+\frac{\partial c\Delta\tau}{\partial z_m}|_{\hat{X}(k/k-1)}(\hat{z}_m(k)-\hat{z}_m(k/k-1)) \\ &+\frac{\partial c\Delta\tau}{\partial \dot{x}_m}|_{\hat{X}(k/k-1)}(\hat{\dot{x}}_m(k)-\hat{\dot{x}}_m(k/k-1)) \\ &+\frac{\partial c\Delta\tau}{\partial \dot{y}_m}|_{\hat{X}(k/k-1)}(\hat{\dot{y}}_m(k)-\hat{\dot{y}}_m(k/k-1)) \\ &+\frac{\partial c\Delta\tau}{\partial \dot{z}_m}|_{\hat{X}(k/k-1)}(\hat{\dot{z}}_m(k)-\hat{\dot{z}}_m(k/k-1)) \end{aligned} \tag{9}$$

where

$$\begin{cases} \frac{\partial c\Delta\tau}{\partial x_m}=\frac{x_1-x_m}{d_{1,m}}-\frac{x_2-x_m}{d_{2m}} \\ \frac{\partial c\Delta\tau}{\partial y_m}=\frac{y_1-y_m}{d_{1,m}}-\frac{y_2-y_m}{d_{2m}} \\ \frac{\partial c\Delta\tau}{\partial z_m}=\frac{z_1-z_m}{d_{1,m}}-\frac{z_2-z_m}{d_{2m}} \\ \frac{\partial c\Delta\tau}{\partial \dot{x}_m}=\frac{\partial c\Delta\tau}{\partial \dot{y}_m}=\frac{\partial c\Delta\tau}{\partial \dot{z}_m}=0 \end{cases} \tag{10}$$

After the above preparation, a random nonlinear lunar rover position system is built up as

$$\begin{cases} \hat{X}(k)=A\hat{X}(k-1)+W(k-1) \\ Z(k)=H(k)dx+V(k) \end{cases} \tag{11}$$

where

$$\begin{cases} A= \\ \begin{bmatrix} \begin{bmatrix} \frac{\cos(w\cdot T\cdot K)-1}{\cos(w\cdot T\cdot(K-1))-1} & 0 & 0 & 0 & 0 & 0 \\ 0 & \frac{\sin(w\cdot T\cdot K)}{\sin(w\cdot T\cdot(K-1))} & 0 & 0 & 0 & 0 \\ 0 & 0 & 1 & 0 & 0 & 0 \\ 0 & 0 & 0 & \frac{\sin(w\cdot T\cdot K)}{\sin(w\cdot T\cdot(K-1))} & 0 & 0 \\ 0 & 0 & 0 & 0 & \frac{\cos(w\cdot T\cdot K)}{\cos(w\cdot T\cdot(K-1))} & 0 \\ 0 & 0 & 0 & 0 & 0 & 1 \end{bmatrix} \end{bmatrix} \\ Z(k)=c\Delta\tau-\left[(d_{2,m}-d_{1,m})-(d_{2,l}-d_{1,l})\right]\hat{X}(k/k-1) \end{cases} \tag{12}$$

$$H(k)=\begin{pmatrix} \frac{\partial c\Delta\tau_{1,2}}{\partial x_m} & \frac{\partial c\Delta\tau_{1,2}}{\partial y_m} & \frac{\partial c\Delta\tau_{1,2}}{\partial z_m} & 0 & 0 & 0 \\ \frac{\partial c\Delta\tau_{1,3}}{\partial x_m} & \frac{\partial c\Delta\tau_{1,3}}{\partial y_m} & \frac{\partial c\tau_{1,3}}{\partial z_m} & 0 & 0 & 0 \\ \frac{\partial c\Delta\tau_{1,4}}{\partial x_m} & \frac{\partial c\Delta\tau_{1,4}}{\partial y_m} & \frac{\partial c\Delta\tau_{1,4}}{\partial z_m} & 0 & 0 & 0 \\ \frac{\partial c\tau_{2,3}}{\partial x_m} & \frac{\partial c\tau_{2,3}}{\partial y_m} & \frac{\partial c\Delta\tau_{2,3}}{\partial z_m} & 0 & 0 & 0 \\ \frac{\partial c\Delta\tau_{2,4}}{\partial x_m} & \frac{\partial c\Delta\tau_{2,4}}{\partial y_m} & \frac{\partial c\Delta\tau_{2,4}}{\partial z_m} & 0 & 0 & 0 \\ \frac{\partial c\Delta\tau_{3,4}}{\partial x_m} & \frac{\partial c\Delta\tau_{3,4}}{\partial y_m} & \frac{\partial c\Delta\tau_{3,4}}{\partial z_m} & 0 & 0 & 0 \end{pmatrix} \tag{13}$$

where $\Delta\tau_{1,2}$ represents the observations obtained at the same time by VLBI antennas 1 and 2, $W(k)$ and $V(k)$ are zero mean white noise sequences, which represent the dynamic noise vector and the measurement noise vector. The statistical properties are as follows:

$$\begin{cases} E(W(k))=0 \\ E(V(k))=0 \\ E(W(k)V^T(j))=0 \\ E(W(k)W^T(j))=Q(k)\delta_{kj} \\ E(V(k)V^T(j))=R(k)\delta_{kj} \end{cases} \tag{14}$$

where $Q(k)$ is the dynamic noise covariance matrix, $R(k)$ is the measurement noise covariance matrix and δ_{kj} is the Kronecker function, as shown in the following:

$$\delta_{kj}=\begin{cases} 1 & (k=j) \\ 0 & (k\neq j) \end{cases} \tag{15}$$

3.2. Kilter parameters in lunar vehicle dynamic positioning

If the initial estimated value $\hat{X}(0)$ and variance P(0) of the Kalman filter meet the following Eq. (16), the filtering process of $\hat{X}(k)$ and $P(k)$ will be unbiased, i.e.

$$\begin{cases} \hat{X}(0)=E(X(0)) \\ P(0)=VAR(X(0)) \end{cases} \tag{16}$$

In essence, if the values of $\hat{X}(k)$ and $P(k)$ are not seriously distorted, $\hat{X}(k)$ and $P(k)$ will gradually get rid of the impact of the initial value for a stable filter with the increase of the filtering time. In the simulation experiment, in order to meet (16), the least squares estimation is used to obtain the initial value and its variance as $\hat{X}(0)$ and $P(0)$. According to the state equation, mainly to ensure the effectiveness of the matrix A, the velocity at the second epoch is selected as the initial velocity, which can be expressed as:

$$\begin{cases} \hat{\dot{x}}_m(0)=RL\cdot\cos(w\cdot T)-RL \\ \hat{\dot{y}}_m(0)=RL\sin(w\cdot T) \\ \hat{\dot{z}}_m(0)=0 \end{cases} \tag{17}$$

where w is the angular velocity, T is the sample interval and the RL is the radius of the moon, and $P_m(0)$ is the error variance of $\hat{X}_m(0)$. If $\hat{X}_m(0)$ is the true required value, the error variance is zero. Since $\hat{X}_m(0)$ is calculated from the sample data, which is accurate, it can be assumed to be equal to the theoretical value, so $P_m(0)$ can be set as the zero matrix.

From experience obtained in several experiments, the covariance matrix of the state vector is set greater than zero, which will enable the filter to have a faster convergence. In this experiment, $P_m(0)$ is set as

$$P_m(0)=\begin{pmatrix} 1\ \text{km}^2 & 0 & 0 & 0 & 0 & 0 \\ 0 & 1\ \text{km}^2 & 0 & 0 & 0 & 0 \\ 0 & 0 & 1\ \text{km}^2 & 0 & 0 & 0 \\ 0 & 0 & 0 & 10^{-12}\ \text{km}^2 & 0 & 0 \\ 0 & 0 & 0 & 0 & 10^{-12}\ \text{km}^2 & 0 \\ 0 & 0 & 0 & 0 & 0 & 10^{-12}\ \text{km}^2 \end{pmatrix} \tag{18}$$

The Kalman filter not only needs to use $\hat{X}_m(0)$ and $P_m(0)$, but also requires the system noise variance $Q(k)$ and the observation noise variance $R(k)$. Given the observed values of the variance and covariance matrices, this will be a true reflection of the system state and will obtain a satisfactory filtering result according to the VLBI observations (Song, 2006). To accurately set the system noise variance and observation noise variance is impossible, and sometimes they cannot be obtained. $Q(k)$ and $R(k)$ are usually determined based on experience or by using the Sage adaptive filtering method. After several experimental comparisons, in this paper,

$R(k)$ takes the values as shown in the following:

$$R(k)_{6\times6} = \begin{pmatrix} (c\cdot\sigma_{vlbi}\cdot10^{-9})^2 & & 0 \\ & \ddots & \\ 0 & & (c\cdot\sigma_{vlbi}\cdot10^{-9})^2 \end{pmatrix} \tag{19}$$

where σ_{vlbi} is the measurement accuracy of the differential VLBI data, and c is the speed of light with 299,792.458 km/s.

The system noise variance matrix $Q(k)$ has nothing to do with the epoch, which needs to be determined according to the characteristics of the dynamic model and should match the accuracy of the dynamic model. If $Q(k)$ is too large, the weighted filter in the previous observations is too large. Therefore, the filter cannot make good use of the existing observations. If the value of $Q(k)$ is too small, with the filtering recursive, more model noise will be introduced so that the filtering error is likely increased or even causes a divergence phenomenon. The value of $Q(k)$ has a significant impact on the filter value of the velocity components. In this paper, $Q(k)$ is set as

$$Q(k)_{6\times6} = \begin{pmatrix} 10^{-10}\ \mathrm{km}^2 & 0 & 0 & 0 & 0 & 0 \\ 0 & 10^{-10}\ \mathrm{km}^2 & 0 & 0 & 0 & 0 \\ 0 & 0 & 10^{-10}\ \mathrm{km}^2 & 0 & 0 & 0 \\ 0 & 0 & 0 & 10^{-12}(\mathrm{km}/s)^2 & 0 & 0 \\ 0 & 0 & 0 & 0 & 10^{-12}(\mathrm{km}/s)^2 & 0 \\ 0 & 0 & 0 & 0 & 0 & 10^{-12}(\mathrm{km}/s)^2 \end{pmatrix} \tag{20}$$

In the model of constant velocity, the time interval between observations will be constant and the transition matrix of the state will be constant. In this condition, the filter matrix of the Kalman filter is dependent on $Q(k)$ and $R(k)$. The solution using the EKF will not be accurate if $Q(k)$ and $R(k)$ are not objective.

The filtering progress is in the moon-fixed coordinate system and the accuracy of the position of the LM can reach 1 km (Li et al., 2010), so a 1 km position error is averagely added to the initial position of the LM and LRV, and the final position is compared to the actual position with no system error.

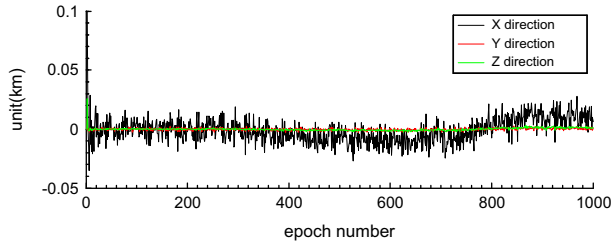

Fig. 2. Position bias between EKF position and actual position.

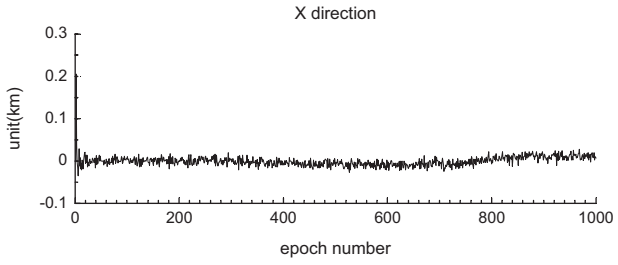

Fig. 3. Position bias between EKF position and actual position in *X* direction.

3.3. The extended Kalman filter

In order to achieve better accuracy of the relative positioning solution, the extended Kalman filtering (EKF) is used in this paper. The process of the extended Kalman filter is showing below.

The one step optimal predicting state is calculated by

$$\hat{X}_{k/k-1} = \hat{X}_{k-1} + f(\hat{X}_{k-1}, t_{k-1})\Delta t \tag{21}$$

The covariance of the one step optimal predicting state is calculated by

$$P_{k/k-1} = \Phi_{k/k-1}P_{k-1}\Phi_{k,k-1}^T + Q_{k-1} \tag{22}$$

The optimal Kalman gain matrix is calculated by

$$K_k = P_{k/k-1}H_k{}^T(H_kP_{k/k-1}H_k{}^T + R_k)^{-1} \tag{23}$$

The optimal filtering state is calculated by

$$\hat{X}_k = \hat{X}_{k/k-1} + K_k[Z_k - h(\hat{X}_{k/k-1}, k)] \tag{24}$$

The covariance of the optimal filtering state is calculated by

$$P_k = (I - K_kH_k)P_{k/k-1}(I - K_kH_k)^T + K_kR_kK_k^T \tag{25}$$

4. Simulation and results

4.1. Numeric simulation

The VLBI stations in Shanghai and Urumqi observed the two satellites of the Japanese lunar probe, Rstar and Vstar (Iwata et al., 2001), with a 25 m radio telescope in 2008. The differential phase delay, with a measurement accuracy ranging from one to several picoseconds (1 ps corresponds to 3 mm), are obtained via same-beam VLBI technology (Kikuchi et al., 2009).

In order to simulate SBI observations, the noises are added. In this paper, differential phase delay observations with initial positioning error, atmosphere delay and random error are simulated. The cycle ambiguity is assumed to be known in the stimulation and the solutions can find in several papers (Liu et al., 2010). For the accuracy of the landing point can reach 1 km (Li et al., 2010), so 1 km initial positioning error is added to the initial position of the LM and LRV in the numeric simulation. The biggest distance between the LM and LRV is just 5 km, which corresponds to

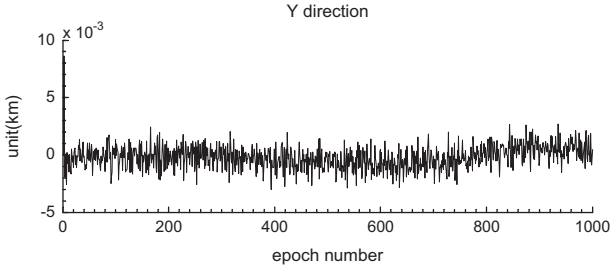

Fig. 4. Position bias between EKF position and actual position in *Y* direction.

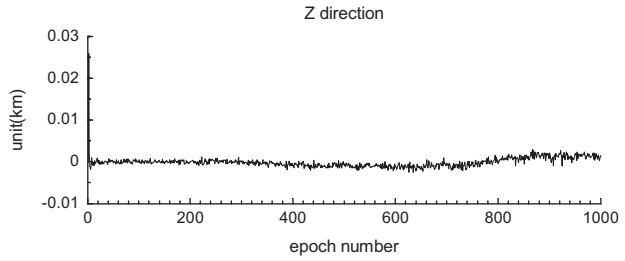

Fig. 5. Position bias between EKF position and actual position in *Z* direction.

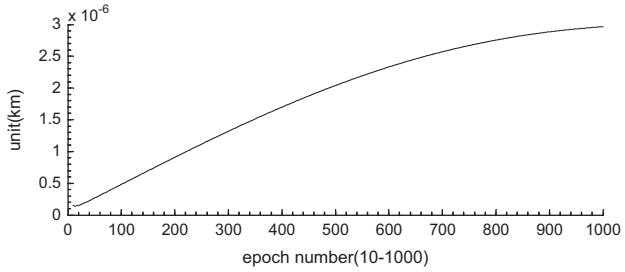

Fig. 6. The variance value corresponding to *X* direction.

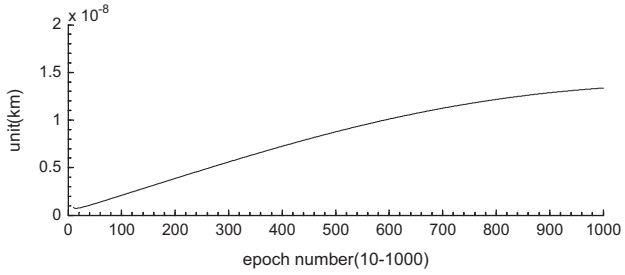

Fig. 7. The variance value corresponding to *Y* direction.

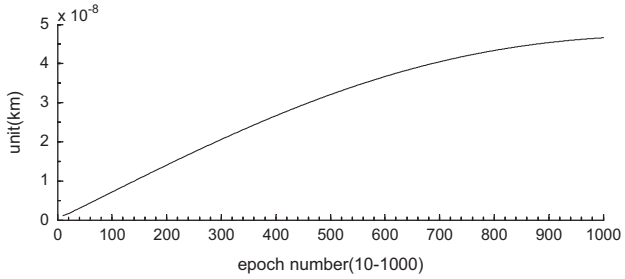

Fig. 8. The variance value corresponding to *Z* direction.

0.000754 rad, the ionosphere delay of SBI is less than 0.1 mm and the atmosphere delay is less than 0.05 mm and the total error caused by ionosphere and atmosphere is less than 0.5 mm (Liu et al., 2010). Te first order ionosphere phase delay of LRV or LM at one VLBI station can be shown as

$$\Delta_{ph}^{Iono} = -\frac{1}{\cos z'}\frac{40.3}{f^2}VTEC \tag{26}$$

where Δ_{ph}^{Iono} is the ionospheric refraction, z' is the zenith angle, f is the frequency of the signal and VTEC represents the vertical total electron content, which can be calculated by the IRI 2007 model (Bilitza and Reinisch, 2008). Here solar flare and geomagnetic storms effects on the ionosphere are not considered (Jin et al., 2008), which should be corrected in real SBI observations. The magnitude of the first order ionosphere delay can be obtained with several centimeters for the frequency of LRV and LM at the four observation stations, which can be eliminated by dual frequency observations. The residual ionosphere delay is less than 10^{-9} m, which is far less than the observation accuracy and can be ignored.

The effect of the neutral atmosphere is denoted as the tropospheric delay, which can be simulated from the Hopfield model at the four observation stations in each epoch. The residual error in the random form, which can be 2% of the whole delay (Kulkarni, 1992), is added in the simulated observation (both the LRV and the LM) to test the influence on the estimation of parameters.

Finally, the random error with zero mean and normal distribution is added to the simulated observations according to the observation accuracy. The random number can be generated by subroutine random with multiplying the expected standard de viation of the observation σ, and the random noise s is yielded. The expected standard deviation of the SBI time delay has been taken 1 ps, 5 ps and 10 ps in this paper. The elevation angle is calculated in using the Hopfield model. Due to the long distance between Earth and moon, the elevation angle varies very little, so it will have very tiny influence on the positioning for choosing different landing point as long as being visible. For brevity, the position vectors of the LRV and the LM are $\vec{r}_m = \vec{r}_1 =$ [1738.0 km 0.0 km 0.0 km] at the first epoch, and then the LRV starts to move with a constant peripheral velocity of 3 cm/s.

4.2. Results derived from EKF

According to the equations listed in Section 3.3, the result is obtained with atmosphere delay, 1 km initial error and 1 ps random error. The biases of the position derived from EKF and the true value in *X*, *Y* and *Z* direction are shown in Fig. 2.

In Fig. 2, we can see that the position in the *Y* and *Z* direction are more stable than that in *X* direction(which is close to the line of sight direction), which may be due to the SBI observation in line of sight direction and the residual effect of the atmosphere errors. Each position bias in *X*, *Y* and *Z* directions is shown in Figs. 3, 4 and 5, respectively.

Table 1
Comparison of the results from least square adjustment, EKF and Adaptive EKF.

Method	Bias								
	Bias in *X* direction			Bias in *Y* direction			Bias in *Z* direction		
	Maximum bias, absolute value (m)	Average bias (m)	RMS (m)	Maximum bias, absolute value (m)	Average bias (m)	RMS (m)	Maximum bias, absolute value (m)	Average bias (m)	RMS (m)
LS	139.40	36.10	45.70	9.20	2.40	3.10	17.70	4.60	5.80
EKF	32.30	−0.28	4.89	1.71	−0.12	0.41	0.85	−0.09	0.31
AKF	6.90	−0.28	1.86	0.97	−0.27	0.33	0.29	0.01	0.09

As we can see, the bias value reaches m-level in X direction, dm-level in Y direction and dm-level in Z direction. The variance value in X, Y, and Z direction derived from EKF are shown in Figs. 6, 7 and 8, respectively.

When the variance information of the three directions is plotted in a single figure, the variance value in the first 10 epochs is several orders of magnitudes bigger than the latter ones and quickly converges to a stable state. The detail information of variance in X, Y and Z direction from 10 to 1000 epochs are shown in Figs. 6–8. As we can see that the variance reaches 10^{-6} km^2 in X direction, 10^{-8} km^2 in Y direction and 10^{-8} km^2 in Z direction.

The velocity biases in the first 1000 epochs reach 10^{-18} km and 10^{-13} km in X and Y directions, respectively and the velocity bias in Z direction is always zero since the transition matrix is diagonal matrix and the initial velocity in Z direction is zero. Though the absolute error in Y direction is five orders of magnitudes bigger than that in X direction, but when comparing the relative error, the values in X direction and Y direction are very close with the same order of magnitude.

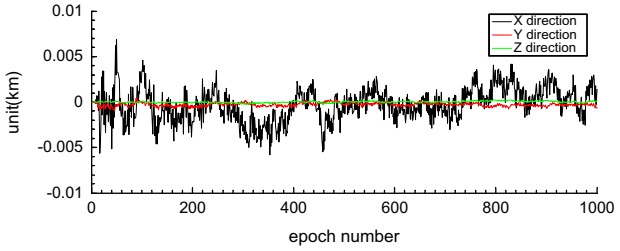

Fig. 9. Position bias between adaptive EKF position and actual position with Initial error of 1 km.

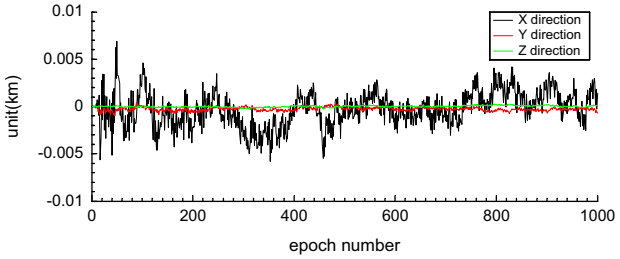

Fig. 10. Position bias between adaptive EKF position and actual position with Initial error of 5 km.

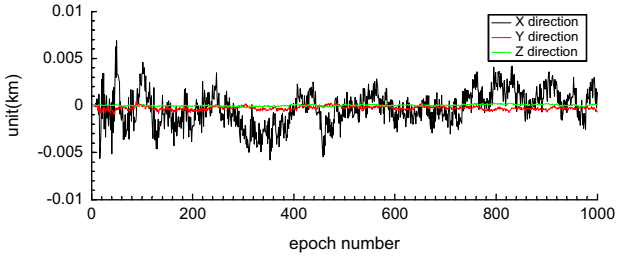

Fig. 11. Position bias between adaptive EKF position and actual position with Initial error of 10 km.

4.3. Comparison of different adjustment methods

After getting the simulated time delay according to the observation function in Section 3.2, the least square adjustment, EKF and adaptive EKF are applied to get the final position and velocity information. Adaptive EKF process is introduced here by comparing with EKF process, the only difference is the gain matrix K_k, which is calculated by

$$K_k = \frac{1}{a_k} P_{k/k-1} H_k^T \left(\frac{1}{a_k} / H_k P_{k/k-1} H_k^T + R_k \right)^{-1} \tag{26}$$

where the symbols are the same with those in Section 3.3 while the adaptive factor is calculated as (Wei et al., 2013):

$$a_k = \left[\frac{tr(\hat{Q}_R)}{tr(Q_R)} \right]^{1/2} \tag{27}$$

Then simulate the same scene as the Section 4.1 and the results from the three different adjustment methods are listed in Table 1, showing the biases between the actual position and the estimated position by the three different adjustment methods.

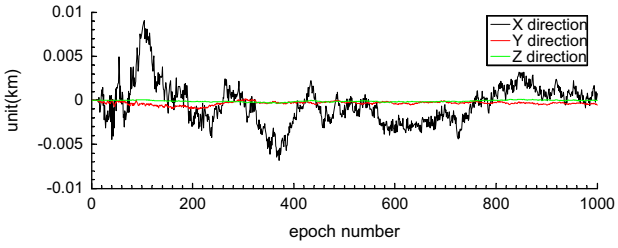

Fig. 12. Position bias between adaptive EKF position and actual position with accuracy of 5 ps.

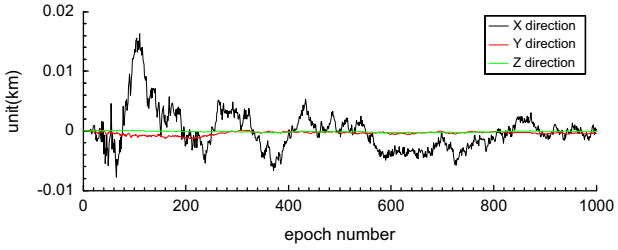

Fig. 13. Position bias between adaptive EKF position and actual position with accuracy of 10 ps.

Table 2
Comparison of the results from Adaptive EKF with different initial errors.

Method (km)	Bias								
	Bias in X direction			Bias in Y direction			Bias in Z direction		
	Maximum bias, absolute value (m)	Average bias (m)	RMS (m)	Maximum bias, absolute value (m)	Average bias (m)	RMS (m)	Maximum bias, absolute value (m)	Average bias (m)	RMS (m)
AKF-1	6.90	−0.28	1.86	0.97	−0.27	0.33	0.29	0.01	0.09
AKF-5	6.90	−0.29	1.87	0.97	−0.27	0.33	0.29	0.01	0.09
AKF-10	6.90	−0.29	1.87	0.97	−0.27	0.33	0.29	0.01	0.09

Table 3
Comparison of the results from adaptive EKF with different initial errors.

Method (ps)	Bias								
	Bias in *X* direction			Bias in *Y* direction			Bias in *Z* direction		
	Maximum bias, absolute value (m)	Average bias (m)	RMS (m)	Maximum bias, absolute value (m)	Average bias (m)	RMS (m)	Maximum bias, absolute value (m)	Average bias (m)	RMS (m)
AKF-1	6.90	−0.28	1.86	0.97	−0.27	0.33	0.29	0.01	0.09
AKF-5	9.07	−0.49	2.40	1.03	−0.33	0.39	0.34	−0.09	0.13
AKF-10	16.3	−0.08	3.50	1.36	−0.39	0.49	0.35	−0.14	0.17

It can be seen that with an accurate dynamic model and a priori statistical knowledge of the parameters, the accuracy of the solution by the EKF and adaptive EKF are better than that with the least squares adjustment. The accuracy of the solutions can reach decimeter in the *X* and *Y* direction and millimeter in the *Z* direction. The accuracy in *Z* direction is the best for LRV's tiny movement in that direction and the assumed initial coordinates of LRV and LM.

Adaptive EKF is widely used nowadays for its better accuracy of the solution and faster convergence. In this experiment, the accuracy of adaptive EKF stays in the same level of accuracy of EKF for the state equation and the observation equation is accurate to greatly weaken the function of the adaptive factor. In addition, the accuracy of Adaptive EKF is better than that of EKF in all three directions, so adaptive EKF performs better in this numerical experiment.

4.4. Comparison of different simulating scenes by adaptive EKF

To test the function of EKF and adaptive EKF in different situations, different scenes are simulated in this section, such as the different initial error and different observation accuracy (random error). In Figs. 9–11, different initial errors (1 km, 5 km and 10 km) are added to the initial position coordinates of LRV and LM, and the other errors are the same as Section 4.2. We can see that the initial bias has little effect on the relative positioning, even when the bias is as large as 10 km, and the positioning bias can be as little as 1 m. The adaptive EKF performs better with a rapid convergence velocity by using adaptive factor.

The detail accuracy of AKF is showing in Table 2. As we can see in Table 2, the results are not affected much by initial errors leveling at several kilometers and the more precise the initial position, the higher the accuracy.

Figs. 12 and 13 show the different random errors with standard deviation 5 ps and 10 ps added to the observation time delay, respectively, while the accuracy of 1 ps is represented in Fig. 9 and the other errors are the same as Section 4.2.

Comparing Figs. 9, 12, and 13, we can see that the random error at the level of several picoseconds has some influence on the relative positioning. When the random error is as large as 10 ps, the maximum positioning bias can be 16.3 m, much bigger than that with random error of 1 ps. The detailed accuracy of AKF is given by Table 3. As we can see that the results are greatly affected by observation accuracy leveling at several picoseconds. The more precise the observation accuracy is, the higher the accuracy of results can be got. So it is important to improve the observation accuracy for positioning.

5. Conclusions

The third phase in the Chinese lunar exploration project intends to gather lunar regolith samples. The LM and LRV on the moon will provide opportunities for the same beam VLBI observation. In this paper, a relative positioning model of lunar rover is presented based on the EKF and SBI. The results of numerical experiments show that the accuracy of the positioning by EKF and adaptive EKF is much better than that by the least squares method, which can achieve the meter level in *X* direction, decimeter level in *Y* and *Z* directions. It need not store amount of passed observation data and the advantage of timely solution when new observations come, the EKF meets the requirements of real-time high precision positioning of LRV. The results are not greatly influenced by the initial positioning error of the landing point, but greatly influenced by the observation accuracy (random error) at the level of several picoseconds. The accuracy of the solution in the *X*-axis is not as good as the *Y*-axis and *Z*-axis, which is due to the character of the VLBI technique with a good restraint in tangent plane, so different observation techniques joined together will compensate the defect in line-of-sight direction. With the continuous progress in lunar exploration, the autonomous navigation of LRV will lead the trend, and the adaptive EKF will play an increasingly important role.

Here the moon is treated as a regular sphere without considering the irregular surface, which in fact will affect the kinematic models and the positioning results finally. Also the antenna system bias and the influence from the lunar environment are needed to further consider. In addition, this paper just simulates and tests the real-time positioning results of Chang'E-3 rover with the same-beam VLBI observations. However, to get the more important details of the moon's interior structure and physical properties, it needs three or more Landers on the moon. In the future, we will further simulate and test the effects of Landers distribution and number on estimates of the moon's interior structure and physical properties.

Acknowledgments

This research was funded by the National '863 Project' of China (No. 2008AA12Z308), National Natural Science Foundation of China (No. 40974003), National Basic Research Program of China (973 Program) (No. 2012CB720000), Main Direction Project of Chinese Academy of Sciences (No. KJCX2-EW-T03) and National Natural Science Foundation of China (NSFC) Project (No. 11173050).

References

Bilitza, D., Reinisch, B., 2008. International reference ionosphere 2007: improvements and new parameters. Advances in Space Research 42 (4), 599–609, http://dx.doi.org/10.1016/j.asr.2007.07.048.

Dong, G., Hao, W., Li, H., Ping, J., Li, J., 2010. Relative positioning of the objectives of the lunar surface by using same-beam Interferometry. Journal of Tsinghua University (Science and Technology) 50 (7), 1118–1124.

Gregnanin, M., Bertotti, B., Chersich, M., Fermi, M., Iess, L., Simone, L., Tortora, P., Williams, J.G., 2012. Same beam interferometry as a tool for the investigation of the lunar interior. Planetary and Space Science 74, 194–201.

Huang, Y., 2006. Orbit Determination of the First Chinese Lunar Exploration Spacecraft CE-1 (Ph.D. thesis), Shanghai Astronomical Observatory. Chinese Academy of Sciences.
Iwata, T., Takahashi, M., Namiki, N., et al., 2001. Mission instruments for lunar gravity field measurements using SELENE sub-satellites. Journal of Geodetic Society of Japan 47, 558–563.
Jin, S.G., Luo, O., Park, P., 2008. GPS observations of the ionospheric F2-layer behavior during the 20th November 2003 geomagnetic storm over South Korea. Journal of Geodesy 82 (12), 883–892, http://dx.doi.org/10.1007/s00190-008-0217-x.
Jin, S.G., 2012. Preface: Recent results on lunar exploration and science. Advances in Space Research 50 (12), 1581–1582, http://dx.doi.org/10.1016/j.asr.2012.09.010.
Jin, S.G., Arivazhagan, S., Araki, H., 2013. New results and questions of lunar exploration from SELENE, Chang'E-1, Chandrayaan-1 and LRO/LCROSS. Advances in Space Research , http://dx.doi.org/10.1016/j.asr.2012.11.022.
Kikuchi, F., et al., 2009. Picosecond accuracy VLBI of the two subsatellites of SELENE (KAGUYA) using multifrequency and same beam methods. Radio Science 44, RS2008, http://dx.doi.org/10.1029/2008 RS003997.
Kulkarni, M., 1992. A Feasibility Study of Space VLBI for Geodesy and Geodynamics[D], Department of Geodetic science and surveying. The Ohio State University, Columbus, Ohio.
Li, J., Guo, L., Qian, Z., 2010. Determination of the controlled landing trajectory of Chang'E-1 satellite and the coordinate analysis of the landing point on the Moon. Chinese Science Bulletin 55 (13), 1240–1245.
Liu, Q., Chen, M., Xiong, W., et al., 2010. Precise relative positioning of the lunar rover based on ultra-high-precision multi-frequency point of same-beam VLBI techniques. Science China Physics, Mechanics and Astronomy 40 (2), 253–260.
Ouyang, Z., 2004. Scientific objectives of Chinese lunar exploration project and development strategy. Advance in Earth Science 19 (3), 351–357. (in Chinese).
Song, Y., 2006. Research on Kalman Filter in Kinematic Positioning (Ph.D. thesis). Central South University, Changsha, China.
Thornton, C., Border, J.S., 2000. Radiometric Tracking Techniques for Deep-Space Navigation. California Institute of Technology, Pasadena, California, USA: Jet Propulsion Laboratory.
Wei, E., Jin, S.G., Zhang, Q., Liu, J., Li, X., Yan, W., 2013. Autonomous navigation of Mars probe using X-ray pulsars: modeling and results. Advances in Space Research 51 (5), 849–857, http://dx.doi.org/10.1016/j.asr.2012.10.009.
Yan, J., Li, F., Liu, Q., Ping, J., Zhong, Z., Li, J., 2011. Proposal of application of same beam VLBI measurements in precision orbit determination of lunar orbiter and return capsule and lunar gravity field simulation in Chang'E-3 mission. Advances in Space Research 48, 1676–1681.